



# Thermo-mechanical characterization and dynamic failure of a CoCrFeNi high-entropy alloy

Longhui Zhang

Department of Engineering Science, University of Oxford, Parks Road, Oxford, OX1 3PJ, UK

## ARTICLE INFO

### Keywords:

High-entropy alloy  
Hopkinson bar  
Thermo-mechanical coupling  
Dynamic shear failure

## ABSTRACT

This paper investigates the thermo-mechanical constitutive relationships of a CoCrFeNi high-entropy alloy (HEA) from quasi-static  $10^{-2}$ /s, medium strain rate of  $10^1$ /s to high strain rates of  $5 \times 10^2$ – $1.1 \times 10^4$ /s. A series of tests, with the use of cylindrical specimen and shear compression specimen (SCS), were performed on a hydraulic Instron machine and a split Hopkinson pressure bar (SHPB) synchronized with a high-speed camera. The temperature rise (self-heating) during medium strain rate deformation is evaluated experimentally. Effects of the environmental temperatures on the dynamic flow response are studied using the SHPB and an environmental chamber. The constitutive relationships of CoCrFeNi HEA present noticeable strain rate and strain sensitivity. This HEA shows exceptional resistance to dynamic shear failure, with an equivalent shear failure strain of about 173%. Microstructural examinations illustrate that the CoCrFeNi HEA fails by adiabatic shear banding. A comparison of dynamic shear flow responses of the CoCrFeNi HEA and eight different metals and alloys is made. This reveals the potential use of HEA in impact resistant applications in aerospace engineering and armour design.

## 1. Introduction

In 2004, Yeh et al. [1] at the National Tsinghua University, and Cantor et al. [2] at the University of Oxford independently published the works of a novel design of multicomponent alloy. Since then, the high entropy alloys (HEAs) have attracted increasing attention in material engineering. The HEA usually consists of four to five components or more elements with an equal molar ratio. A series of excellent properties of the HEA have been discovered, such as the exceptional properties at low and high temperatures [3], high fracture toughness [4], and good resistance to fatigue and wear [5,6].

Available studies of HEAs, which focus on the mechanical characterization at quasi-static loading and room temperature, are documented in Refs. [7,8]. The HEAs potentially used in the practical structures would experience the impact loading. The mechanical properties of materials are strain rate and temperature dependent [9–12]. It's widely accepted that a strain rate of  $10^3$ /s significantly influences the deformation and failure of metallic alloys [11,13]. The materials under impact show different mechanical responses compared to the quasi-static loading. He et al. [14] carried out a series of dynamic compressive tests for FeCoNiCrMn HEA at room temperature and strain rate of 2100/s using the SHPB technique [15–17], and evaluated its

dynamic response and the underlying deformation mechanism. Park et al. [18] investigated the deformation and microstructural evolution of CoCrFeMnNi HEA at high strain rates of 3000–4000/s. Ma et al. [19] reported the mechanical properties of the AlCrCuFeNi HEA at quasi-static and high strain rates of 1000–3000/s and room temperature. The dynamic constitutive behaviour was analysed using the Johnson-Cook model. Recently, Zhang et al. [20] studied the constitutive properties and strain rate strengthening mechanisms of TiZrHfNb-TaMo HEAs under dynamic compression at strain rates of 2100–6000/s. Studies of the ultra-high strain rate strengthening in the refractory HEA would be important to the prospective application. As indicated by Kumar et al. [21], the strain rate dependent yield strength and work hardening are the main characteristics of HEA during the dynamic deformation at room temperature.

Recently, the use of HEA in ballistic protection was reported by Tudor et al. [22] and Geantă et al. [23]. Muskeri et al. [24] showed that the ballistic impact of HEA involved complex thermo-mechanical and failure processes. The combined strength, strain hardening and ductility enabled the HEA to resist shear localization during intensive impact. Meyer and Li [25,26] studied the shear localization of HEA materials at strain rate of 1800/s, using the hat-shaped specimen and the SHPB technique. No adiabatic shear band occurred even at a shear strain larger

E-mail addresses: [lhzhang.mechanics@gmail.com](mailto:lhzhang.mechanics@gmail.com), [longhui.zhang@eng.ox.ac.uk](mailto:longhui.zhang@eng.ox.ac.uk).

<https://doi.org/10.1016/j.msea.2022.143166>

Received 22 February 2022; Received in revised form 11 April 2022; Accepted 16 April 2022

Available online 18 April 2022

0921-5093/© 2022 The Author. Published by Elsevier B.V. This is an open access article under the CC BY-NC-ND license (<http://creativecommons.org/licenses/by-nc-nd/4.0/>).

than 100%. Consequently, the HEA materials, with remarkable resistance to shear localization, would be potentially used in the armour design [22,23,27].

Although the strain rate of  $10^3/s$  can be achieved by the SHPB technique, this strain rate would be one order of magnitude lower than that experienced in impact events, such as the impact of debris [28,29], bird strike [30] and blade off [31,32] in aerospace engineering. The literature shows two gaps, which cannot be easily achieved using the conventional specimen or the SHPB technique, exist in the constitutive characterization of the HEA materials at strain rates of  $10^1/s$  and  $10^4/s$ . The shear compression specimen (SCS) designed by Rittel [33–35] would allow the large strain testing of HEAs at high strain rates of  $10^4/s$ – $10^5/s$ . The potential tougher structural design using HEAs requires a better understating of the flow behaviour over wider ranges of strain rates, including medium strain rate of  $10^1/s$  and higher strain rate of  $10^4/s$ . Recently, Peng et al. [36] and Li et al. [37] studied the responses of HEAs at very high strain rates of  $10^6$ – $10^{10}/s$  and different temperature conditions using molecular-dynamics. It's found that the temperature and strain rate significantly affect the plastic deformation mechanisms of HEAs. The molecular dynamics simulation was also used by Xie et al. [38] to investigate the local chemical fluctuations in entropy alloy at very high strain rates and different temperature conditions. The strain rate and temperature are the main factors influencing the mechanical behaviour of metallic alloys. The experimental evaluation of temperature on the dynamic flow of HEA is important. In addition, as a typical dynamic failure mechanism, the adiabatic shear band (ASB) indicates the uncontrollable failure proceeds by shear strain localization [39–42]. Large local strain and high temperature are expected to develop inside the ASB. Compared to the documented studies of ASB of a series of metallic alloys [39,42–44] in the past several decades, the investigation of ASB in HEA materials is insufficiently explored.

In this paper, assisted by the Digital Image Correlation (DIC) technique [45–47], the constitutive relationship of a CoCrFeNi alloy, which is selected as a typical model HEA, is measured from quasi-static 0.01/s to high strain rate of 11,000/s. Dynamic shear localization of the CoCrFeNi HEA is investigated using the SCS specimen. This study will provide useful data for engineering applications and the impact resistant alloy design. The material, specimens, and testing techniques are presented in Section 2. Section 3 shows the experimental results. Section 4 discusses the main thermo-mechanical characteristics of the CoCrFeNi alloy, followed by the conclusion.

## 2. Experimental protocol

### 2.1. Material and specimens

The CoCrFeNi alloy consisting of four components with equal molar ratio is fabricated using the vacuum levitation melting technique [48, 49]. The material is supplied as a rod shape with 10 mm diameter. The initial microstructure of CoCrFeNi HEA is characterized using EBSD under the scanning electron microscope (Zeiss EVO 15LS). The sample was sectioned along the axial direction of the material bar and was polished using the alumina suspension. The working voltage of SEM is 15 kV, with the inclination angle of the specimen being  $70^\circ$  and the step size of 2–3  $\mu m$  for EBSD analysis. The EBSD map in Fig. 1 shows that the CoCrFeNi HEA crystallizes in the FCC structure with a grain size of about 92  $\mu m$ , which is similar to the CoCrFeNi alloy in Refs. [50,51].

The compression tests were carried out using a cylindrical specimen. The diameter and the length are both equal to 3 mm. The SCS specimen was adopted to characterize the flow behaviour of CoCrFeNi alloy at high strain rate of  $10^4/s$ . The SCS [35,40] is a cylinder with an inclined semi-circular gauge section which is manufactured at  $45^\circ$  with respect to the axial direction. Fig. 2 shows the geometry of SCS, and Fig. 3 shows a real image of the cylindrical specimen and SCS. The SCS [52,53] enables the large strain testing up to failure at high strain rates.

The data reduction of SCS comprises the finite element simulation

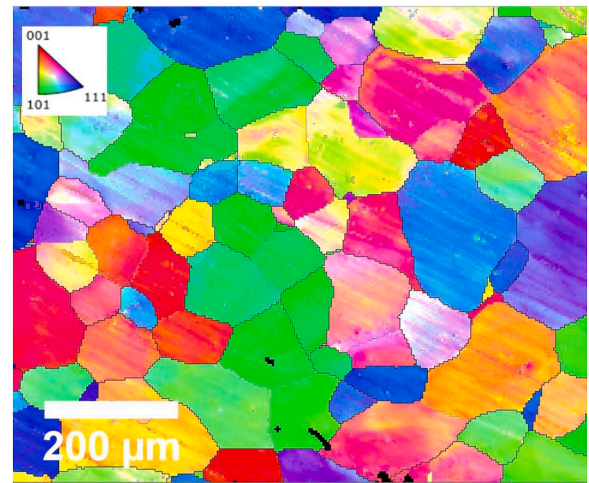


Fig. 1. Initial microstructure of CoCrFeNi HEA from EBSD map.

using a commercial software ABAQUS [54]. The experimental load-displacement data at the specimen ends is transferred to the equivalent stress-strain relationship in the gauge section [55–57]. The formulations are given by:

$$\epsilon_e = \epsilon_y + \sum_{i=1}^N K_{i+2} \left( \frac{d - d_y}{h} \right)^i \quad (1)$$

$$\sigma_{Mises} = K_1 (1 - K_2 \epsilon_e) \frac{P}{D t} \quad (2)$$

where  $\sigma_{Mises}$  and  $\epsilon_e$  are the equivalent stress and strain,  $h$  and  $t$  are the height and the thickness of gauge section,  $D$  is the specimen diameter.  $d$  and  $P$  correspond to the relative vertical displacement and the force at the specimen ends. Here,  $d_y$  and  $\epsilon_y$  are the displacement and strain values at the yield point. With the assistance of finite element simulation, the coefficients to transfer the force to the equivalent stress are  $K_1 = 0.9200$ ,  $K_2 = 0.2031$ . The coefficients to transfer the relative vertical displacement to the equivalent strain of CoCrFeNi alloy, through the polynomial fitting using Matlab, are  $K_3 = 3.1957$ ,  $K_4 = -18.3737$ ,  $K_5 = 74.2506$ ,  $K_6 = -140.9775$ ,  $K_7 = 126.4513$ ,  $K_8 = -43.5453$ .

### 2.2. Experimental setup

The compression tests at quasi-static and medium strain rate were carried out using a hydraulic Instron machine 8850. A K-type thermocouple was welded on the central surface of the cylindrical specimen, in order to reveal the temperature change during the deformation at medium strain rate. The temperature was recorded at a sampling rate of about 2500 fps, using a thermocouple amplifier FE-386-TC<sup>1</sup> connected to the Tektronix DPO 3034 digital oscilloscope. The hydraulic machine was programmed to apply the compressive loading to the grease lubricated specimen under displacement control mode, at constant speeds of 0.03 mm/s and 30 mm/s respectively. These velocities correspond to the compressive loading at quasi-static 0.01/s and medium strain rate of  $10^3/s$ . To avoid damage to the load platens, the tungsten carbide anvils were placed between the specimen and the load platens. A phantom camera and a commercial DIC software (Lavisision Davis<sup>2</sup>) were used to measure the engineering strain of the cylindrical specimen, from the relative displacement of the tungsten carbide anvils painted with speckle pattern. This is a methodology adopted in the author's recent works

<sup>1</sup> Fylde Electronic Laboratories Ltd, 49/51 Fylde Road, Preston, Lancashire PR1 2XQ, UK.

<sup>2</sup> LaVisionUK Ltd, 2 Minton Place Victoria Road, Bicester OX26 6QB, UK.

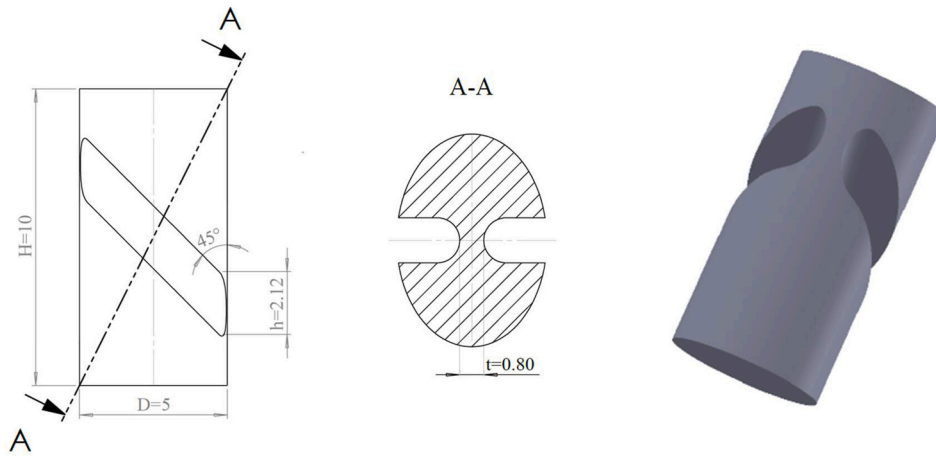


Fig. 2. Drawing of SCS with the unit of mm.

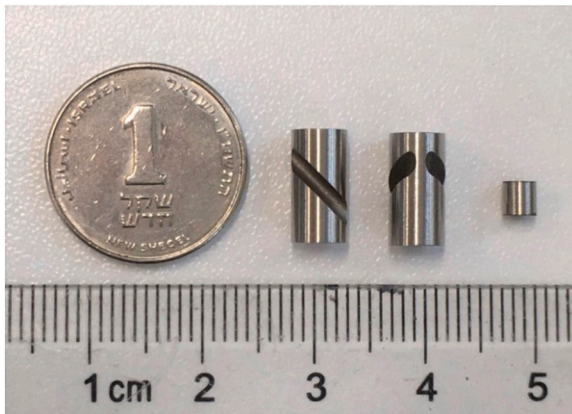


Fig. 3. Image of the SCS and cylindrical specimen, together with a new Israeli shekel coin (18 mm diameter) for a comparison of the size.

[58–61].

Tests at high strain rates were performed on a bespoke 16 mm diameter SHPB apparatus [58,59,62]. The 2.7 m long incident and transmitted bars were made from Ti6Al4V alloy. The 2.5 m long striker bar was also made from Ti6Al4V alloy. Fig. 4 schematically shows the SHPB setup. A slightly grease lubricated specimen is sandwiched between the incident and transmitted bars. A high speed camera (Kirana camera<sup>3</sup>) was synchronized, with the image resolution of  $924 \times 748$  pixels at a frame rate of 100,000 fps. In addition to the tests at room temperature, the tests at 100 °C and 200 °C were carried out using an environmental chamber. The high speed images were processed by Lavision Davis for the DIC analysis. The matching was based on a 6th order spline sub-pixel image interpolation scheme and an affine shape function [63].

Two sets of strain gauge (Gauge 1 and 2) were bonded on the incident bar to separate the superimposed waves. This is because the length of the striker bar is comparable to the length of the incident bar. Typical strain gauge signals of the SCS specimen are shown in Fig. 5a. The boundary force and displacement histories were measured by the classical SHPB analysis [64,65]. Details of the stress wave analysis can be found in Refs. [59,66]. Fig. 5b shows the comparison of the input and output forces, together with a constant velocity during dynamic deformation. The high speed impact results in a noisy initial part in the input force, which is due to the radial oscillation of the incident bar

(Pochhammer oscillation [67,68]). Dynamic force equilibrium can be observed in the plastic deformation region. The force and the stress of the specimen can be measured based on the output force.

### 3. Experimental results

#### 3.1. Results at quasi-static and medium strain rate

The quasi-static true stress-strain curves of CoCrFeNi HEA are shown in Fig. 6, together with the comparison to those at medium strain rate of 10/s. The quasi-static yield stress is about 280 MPa. The medium strain rate increases the yield stress to a higher value of about 310 MPa. Beyond a true strain of 0.5, the flow stress at medium strain rate is lower than that at quasi-static loading. Fig. 7 typically shows the stress histories at quasi-static and medium strain rate, together with the corresponding temperature measurements. The temperature rise of the specimen is about 1.5 °C under quasi-static condition. However, the temperature rise of the specimen increases to 78 °C at medium strain rate, followed by the cooling down due to the unloading. This indicates the deformation of CoCrFeNi alloy at medium strain rate is associated with a temperature change, which is different from that at quasi-isothermal loading with negligible temperature increase.

#### 3.2. Results at high strain rates

Fig. 8 presents the true stress-strain relationships at strain rates of 700–2700/s and room temperature. The determination of approximate yield stress is illustrated in Fig. 8. The flow stress values at strain rates of 2400–2600/s are only slightly higher than that at strain rate of 700/s. The stress-strain curves show an initial noise due to the high frequency Pochhammer oscillation [67,68]. They become relatively smooth beyond a true strain of 0.2. Fig. 9 shows the high speed images of the compressive deformation process at strain rate of 2400/s. From the DIC analysis, the uniform deformation can be observed during the test. A slight strain concentration exists at two ends of the specimen.

Fig. 10 summarizes the true stress-strain relationships of the CoCrFeNi in the present work and the HEAs from the recent literature [20,21,25] at high strain rates of about 2000/s. The  $\text{Al}_{0.1}\text{CoCrFeNi}$  HEA presents the lowest flow stress. The CoCrFeNi, CrMnFeCoNi and  $\text{Al}_{0.3}\text{CoCrFeNi}$  alloys show comparable flow stress. However, the CoCrFeNi shows more significant strain hardening. In addition, as a refractory HEA, the  $\text{TiZrHfNbTaMo}_{0.75}$  presents the highest flow stress above 1760 MPa, with a sacrifice of strain hardening. From the comparison in Fig. 10, one can find that the CoCrFeNi HEA shows an excellent combination of flow stress and work-hardening during dynamic deformation.

<sup>3</sup> Specialised Imaging Ltd., 6 Harvington Park, Pitstone LU7 9GX, UK.



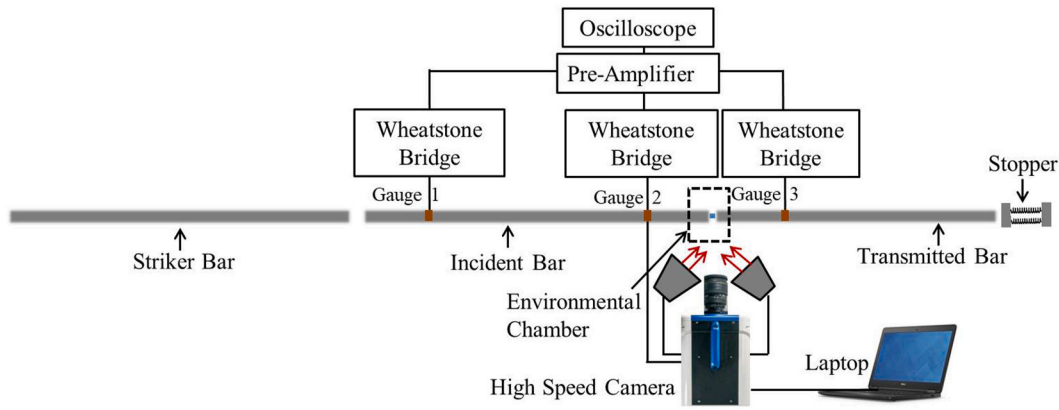


Fig. 4. Schematic of the Hopkinson bar apparatus for the tests at high strain rates.

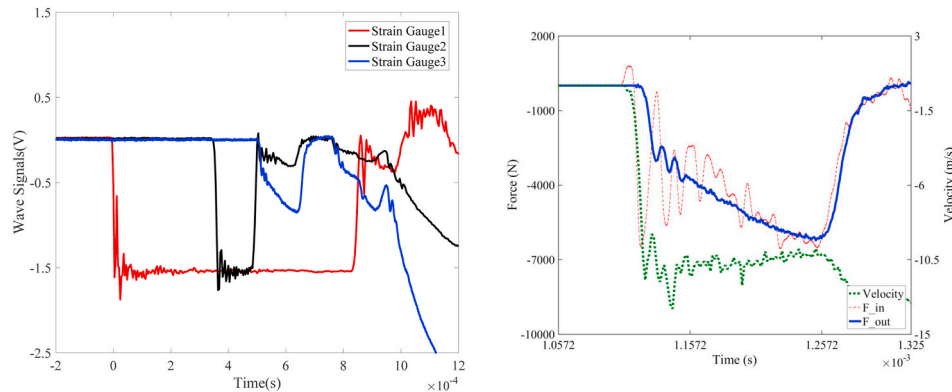


Fig. 5. Typical measurements using the SHPB (a) Strain gauge signals (b) Force equilibrium with a constant boundary velocity.

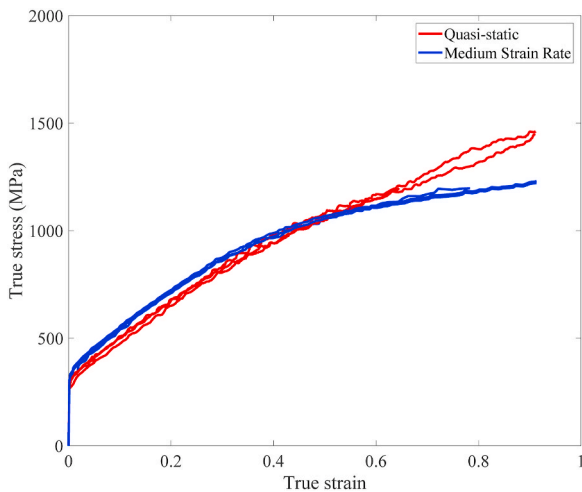


Fig. 6. True stress-strain relations of CoCrFeNi HEA at quasi-static (shown in red color) and medium strain rate (shown in blue color). (For interpretation of the references to color in this figure legend, the reader is referred to the Web version of this article.)

Fig. 11 compares the true stress-strain relationships at strain rate of 2500/s at room temperature and elevated temperatures. At a given strain of 0.08, a moderate decrease of flow stress from 577 MPa to 470 MPa can be seen from room temperature to 200 °C. At a given strain of 0.4, the flow stress decreases from 1010 MPa at room temperature, 880 MPa at 100 °C to 760 MPa at 200 °C. The temperature effect on the flow stress is more apparent with the increase of strain. The compressive

deformation process at strain rate of 2500/s and 200 °C can be observed from the high speed images in Fig. 12. Except for a slight strain concentration at two ends, most of the specimen experiences a uniform deformation at elevated temperature.

The dynamic true stress-strain relationships of SCS are shown in Fig. 13a, together with the counterparts of cylindrical specimens. With the use of SCS, the constitutive relationships at high strain rates of about 11,000/s can be measured. Although there is an initial oscillation, it's clear that the flow stress, at a true strain of less than 0.2, increases with the increase of strain rate. The lowest flow stress appears in the true stress-strain curve at strain rate of 700/s. With further deformation, the stress-strain curves at strain rate of 10,000/s overlap with those at strain rate of 2600/s. This indicates the CoCrFeNi alloy shows both strain rate and strain dependant flow behaviour. Fig. 13b shows that the failure strain of CoCrFeNi is about 1.0. Based on the von Mises theory, this corresponds to an equivalent shear strain of 1.732 ( $\gamma_e = \sqrt{3}\epsilon_e$ ).

The SCS allows large strain testing up to the failure. The initial SCS of CoCrFeNi HEA before the test is shown in Fig. 14a, with the 45° inclined semi-circular gauge section being in front of the high speed camera. As can be seen in Fig. 14b, the SCS enables the dominant shear deformation of CoCrFeNi alloy and the failure at the centre of gauge section. Such a large strain shear deformation shown in Figs. 13 and 14 indicates a strong resistance to dynamic shear failure.

The strain rate dependent flow stress of CoCrFeNi alloy at a given true strain of 0.11 is shown in Fig. 15. Specifically, the flow stress increases from 510 MPa at quasi-static to 570 MPa at medium strain rate and 640 MPa at high strain rate of 11,000/s. The dependence of the flow stress on the strain rate is described by a power law model, which is defined as:



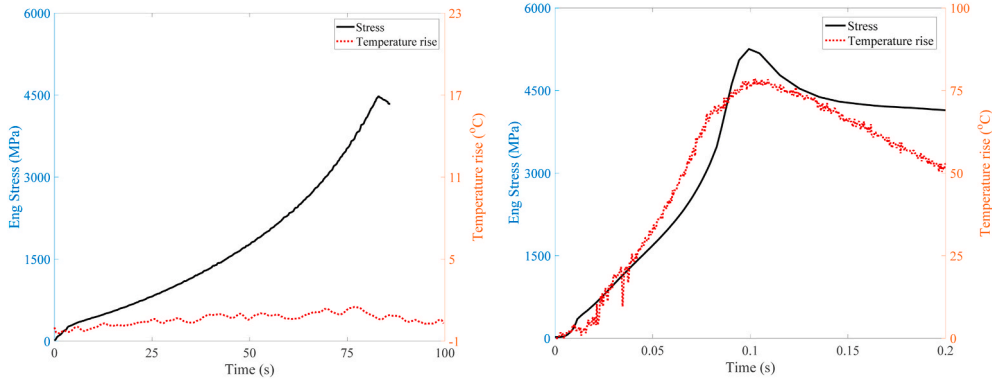


Fig. 7. Real time stress and temperature histories of CoCrFeNi alloy at (a) quasi-static and (b) medium strain rate.

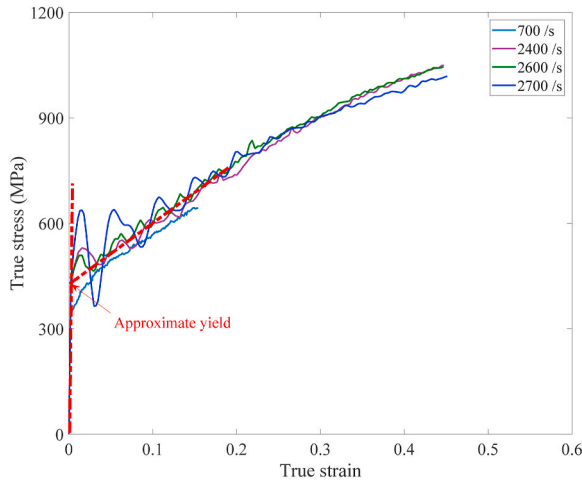


Fig. 8. True stress-strain curves of CoCrFeNi HEA at strain rates of 700–2700/s. Two linear dashed lines assist in the determination of dynamic yield approximately.

$$\sigma = \sigma_{ref} \left( \frac{\dot{\epsilon}}{\dot{\epsilon}_{ref}} \right)^c \quad (3)$$

where  $\sigma_{ref}$  is the reference flow stress,  $\dot{\epsilon}_{ref}$  is the reference strain rate of 0.01/s, the parameter  $C$  reveals the strain rate dependence with the increase of strain rate  $\dot{\epsilon}$ . Fig. 15 compares the experimental data and the model description across a series of strain rates. The simple model  $\sigma = 510 \left( \frac{\dot{\epsilon}}{0.01} \right)^{0.0162}$  can describe the strain rate dependent flow stress of CoCrFeNi HEA at room temperature.

The dynamic deformation of CoCrFeNi HEA is associated with adiabatic self-heating. Assuming the adiabatic condition, the integration of the transient stress-thermal balance equation [69], while neglecting

thermoelastic couplings, results in

$$\beta_{int} \int_0^{\alpha} \sigma d\epsilon_p = \rho c_p \Delta T \quad (4)$$

where  $\beta_{int}$  is the Taylor-Quinney factor [70–73],  $\rho$  is the material density,  $c_p$  is the specific heat and  $\Delta T$  is the temperature rise due to the thermo-mechanical coupling. Here, the measured density of about 7800 [kg/m<sup>3</sup>] and the specific heat 460 [J/kg · K] [26,74,75] are the typical parameters for the CoCrFeNi HEA. A series of experimental measurements show that, the Taylor-Quinney factor depends on the material and the loading mode, and would be far away from 0.9, see Rittel et al. [71], MacDougall [72,73] and Zhang et al. [76]. The  $\beta_{int}$  factor of 0.9 is

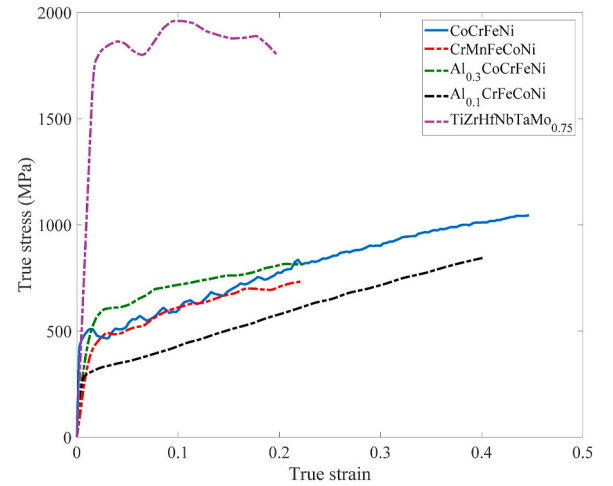


Fig. 10. Dynamic constitutive responses of current CoCrFeNi HEA and the HEAs in the recent literature [20,21,25].

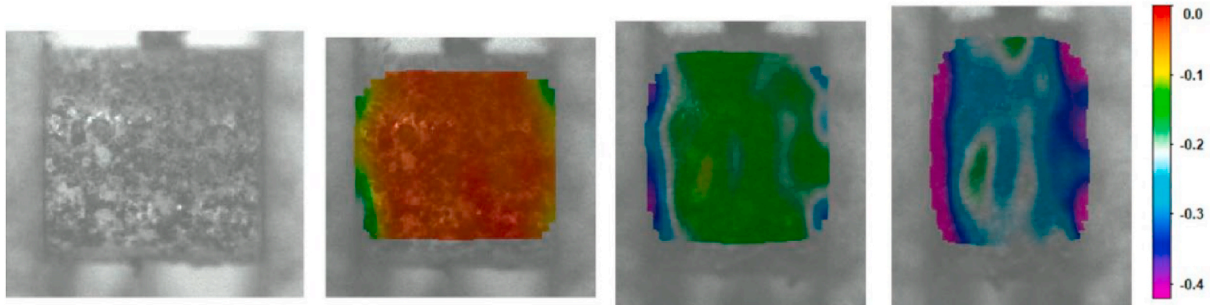


Fig. 9. High speed images of the compressive deformation at strain rate of 2400/s. (The contour is the axial engineering strain from DIC analysis).

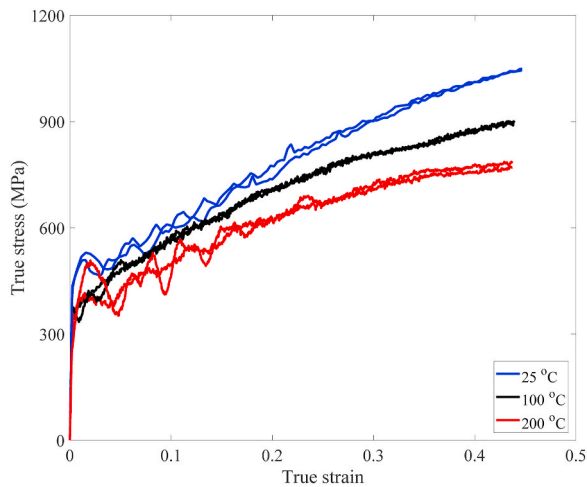


Fig. 11. Comparison of true stress-strain curves at 2500/s from room temperature to 200 °C.

adopted here, in order to estimate a *maximum* temperature rise [34,53,77] during the large strain shear testing. Such a calculation of temperature rise of HEAs at dynamic loading can be found in Wang et al. [78] and Zhang et al. [20]. Fig. 16 shows the temperature rise as a function of true strain at high strain rates of about 10,000/s for the CoCrFeNi alloy. The temperature rise increases with the increase of strain. The estimated *maximum* temperature rise at the load drop is about 230 °C. The specimen temperature above 200 °C causes a thermal effect to the constitutive relationship. Here, it's stated that the temperature rise influences the dynamic flow stress of CoCrFeNi alloy, instead of pointing out the temperature rise results in the shear failure, given that the dynamic constitutive relationship at elevated temperature of 200 °C still shows good deformability (Fig. 11).

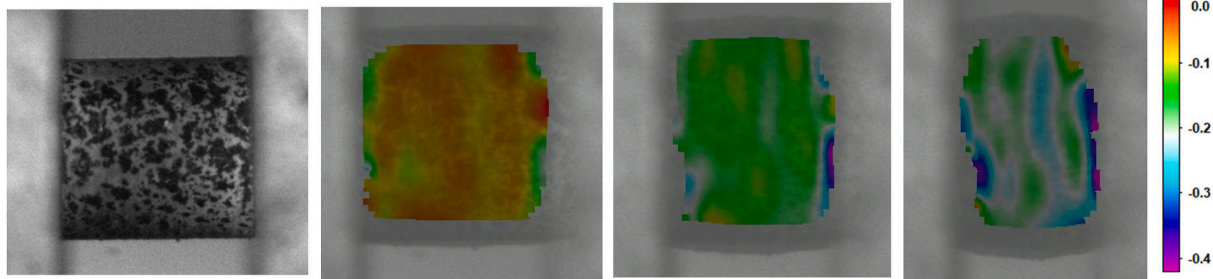


Fig. 12. Compressive deformation at strain rate of 2500/s and elevated temperature of 200 °C. (Axial engineering strain contour from DIC analysis is shown).

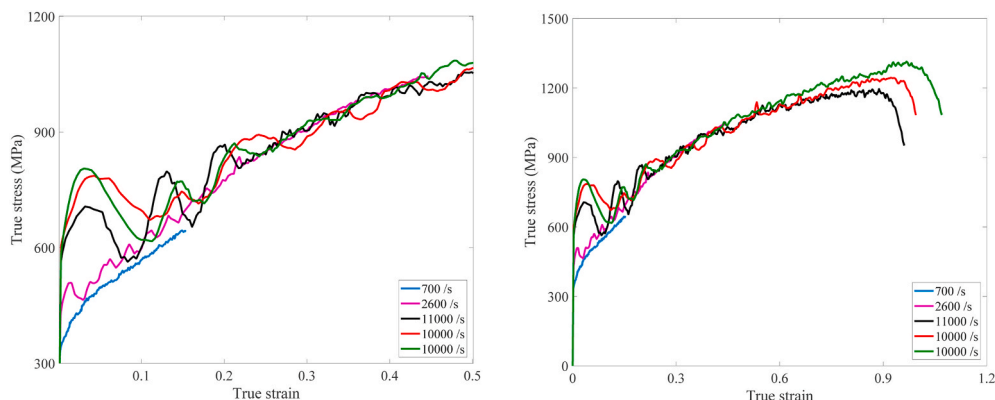


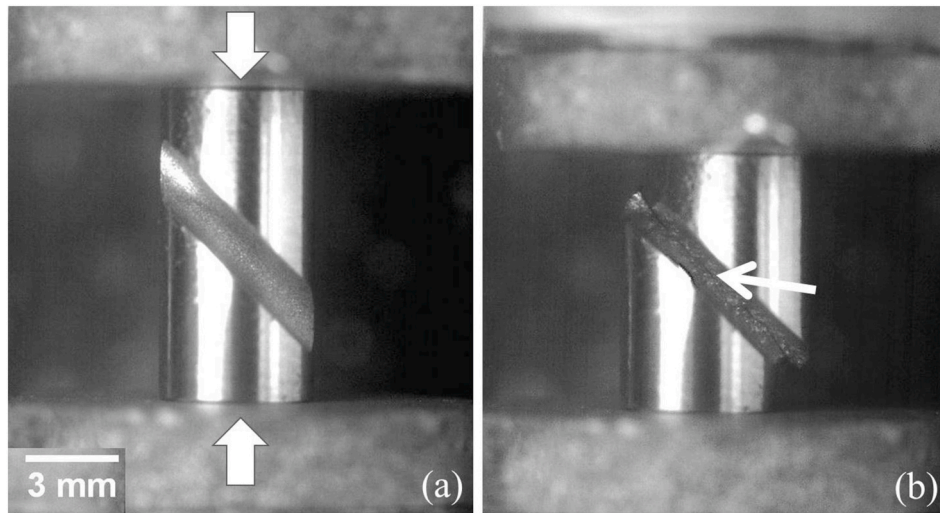
Fig. 13. Dynamic true stress-strain curves of SCS (a) Comparison with the cylindrical specimens (b) True stress-strain curves of SCS up to failure.

Fig. 17 compares the dynamic shear flow of the CoCrFeNi alloy and other aircraft alloys reported by Rittel et al. [71] and Zhang et al. [58,76], in order to illustrate whether there is a potential use of CoCrFeNi alloy in aerospace engineering [79] and armour design. The alloys are ranging from soft aluminium (Al) alloys to a full hardened Maraging C300 steel. They are three Titanium alloys (Ti6Al4V alloy, Commercial Pure Titanium, Ti3Al2.5V alloy), two aluminium alloys (Al2024 and Al5086) and three types of steel (1020 steel, 304L stainless steel and C300 Maraging steel). A first observation is that the failure strain of CoCrFeNi alloy is significantly higher than that of other alloys (flow curves of 1020 steel and Al 5086 without failure), indicating the remarkable shear resistance of this HEA. Likewise, the yield stress of CoCrFeNi HEA is similar to that of 1020 steel, but the strain hardening of CoCrFeNi HEA is stronger than that of 1020 steel. Although the flow stress of CoCrFeNi is not as high as titanium alloys, a significant strain hardening can be seen in the dynamic shear flow of CoCrFeNi HEA.

Evaluation of the impact energy absorption (strain energy density up to failure) of metallic alloys would be of interest to the designers. Fig. 18 compares the energy absorption of various alloys as a function of the density. The CoCrFeNi alloy shows the highest energy absorption in the highest density group. Titanium alloys with a lower density also show good energy absorption capacity. Although the Al 2024 shows the lowest energy absorption, the low weight property makes it unique in the aircraft industry. Consequently, the CoCrFeNi HEA presents a potential use in impact resistant applications in aerospace engineering [79] and also armour design [27], where the HEA could be a good replacement for some steel materials.

### 3.3. Microstructural characterization

The dynamically shear failed microstructures of CoCrFeNi alloy are characterized using SEM and EBSD. Fig. 19a shows a distinct localization zone, indicating the microstructure experiences intensive shear deformation. The micro cracks (square) along the ASB (arrow) can be



**Fig. 14.** Image of SCS of CoCrFeNi HEA (a) before deformation (b) after dynamic deformation. In the image, the incident bar locates at the top of the specimen. The loading directions are marked by two white color filled arrows in (a). The shear failure is marked by an arrow in (b).

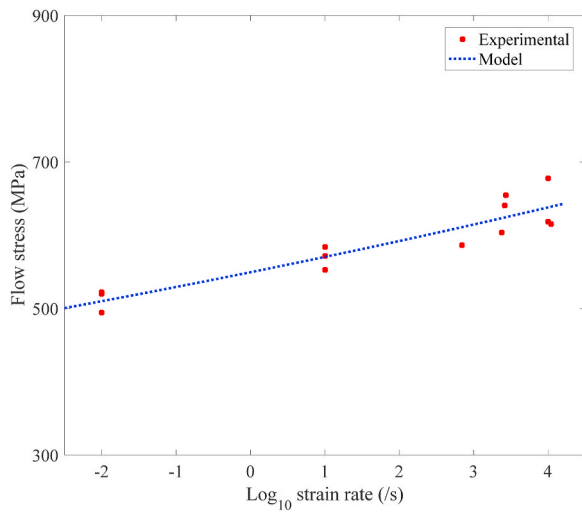


**Fig. 15.** Flow stress of CoCrFeNi at different strain rates, and the description from the power law model.

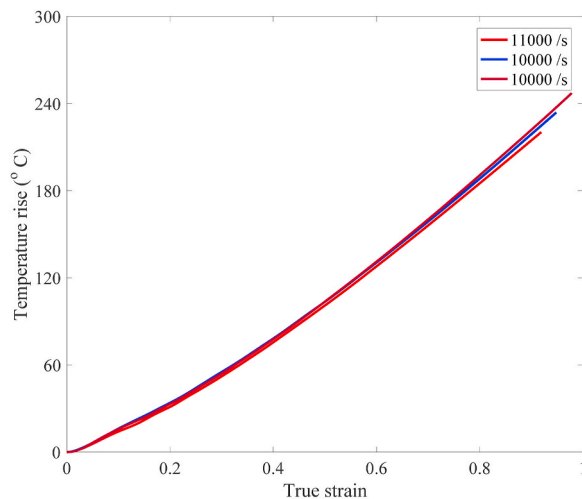


**Fig. 16.** Estimated *maximum* temperature rise as a function of true strain of CoCrFeNi alloy in dynamic shear testing.

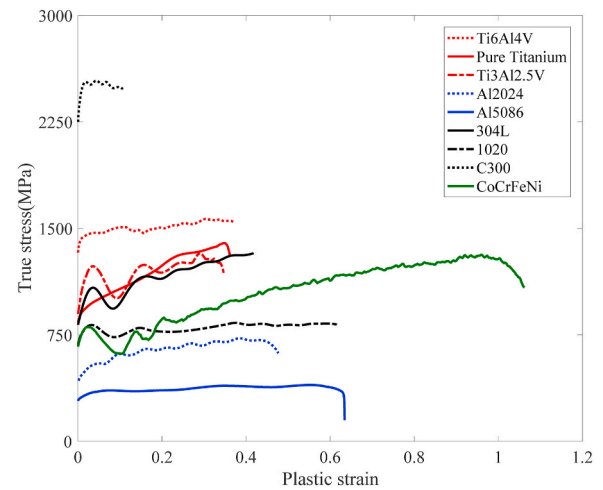


**Fig. 17.** Comparison of the dynamic shear flow of the current CoCrFeNi HEA and other metals and alloys studied by the author [58,71,76]. Note that the titanium alloys are lightweight alloys widely used in aerospace engineering.

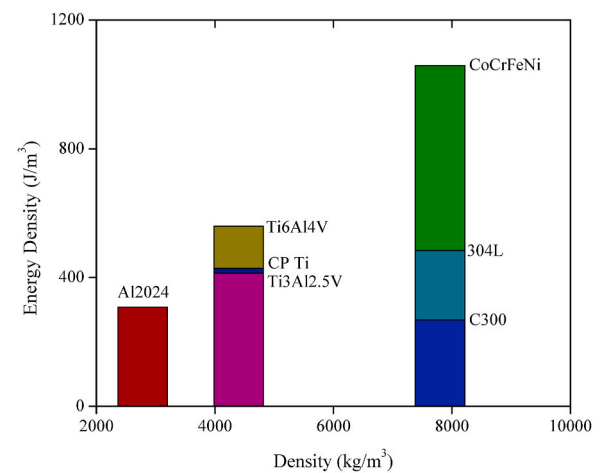


**Fig. 18.** Comparison of the energy absorption vs. density of the current CoCrFeNi HEA and other metals and alloys studied by the author [58,71,76]. Three representative groups of Al alloy, Titanium alloy and steel are shown.



observed. The width of ASB of CoCrFeNi alloy ranges from 35 to 100  $\mu\text{m}$ , which is similar to the relatively wide ASB width (about 100  $\mu\text{m}$ ) in the structural steels [80,81]. The shear fracture surface is shown in Fig. 19b. The dimples are surrounded by severe shear facets. Less elongated dimples (dotted arrow) and significantly elongated dimples (dashed arrow) are evenly distributed in the fracture surface. These are similar to the previous microstructural characterizations with adiabatic shear failure mode [44,82].

In addition, the microstructure of the CoCrFeNi alloy is characterized using EBSD. Fig. 20a shows the EBSD map of CoCrFeNi alloy with ASB, which is a magnified image of that in Fig. 19a. Due to the step size and the shear deformation within ASB with a very fine microstructure, no orientation data can be acquired in the dark area [83]. In the transition zone adjacent to the ASB, the grains elongate along the shear direction. The CoCrFeNi HEA undergoes shear localization in large strain shear testing, indicating the highly localized characteristic of its dynamic failure mechanism. Fig. 20b shows the significant inhomogeneous shear deformation close to the fracture surface. Although the finer microstructures inside the ASB is relatively difficult to acquire [84], it is clear that, the localized deformation within ASB and the associated micro cracks result in the dynamic shear fracture of CoCrFeNi HEA at high strain rates.

#### 4. Discussion

The HEAs [1,2] have gained increasing attention in recent years. The further development of novel HEAs requires mechanical characterization at different strain rates (and temperatures). This paper studies the thermo-mechanical behaviour of a CoCrFeNi HEA and the dynamic failure in large strain shear testing. Likewise, the constitutive relationship is characterized from quasi-static loading to high strain rates. In the literature, two gaps exist at strain rates of  $10^1/\text{s}$  and  $10^4/\text{s}$ , in the measurement of constitutive response of HEAs. The experimental studies of temperature effect on the dynamic flow of HEAs are also less reported. Compared to the documented ASB studies of the traditional metallic alloys, the investigation of HEAs is insufficient. The main results of this work are summarized as follows:

The flow stress of CoCrFeNi HEA increases from quasi-static, medium strain rate to high strain rates, and the dependence of the flow stress on the strain rate can be described by a power law model. The dynamic compression tests at elevated temperatures show the reduced flow stress with the increase of temperature to 200  $^{\circ}\text{C}$ . Consequently, the stress-strain relationships of CoCrFeNi alloy are strain rate and temperature dependent. This statement agrees with the recent studies of Peng et al. [36] and Li et al. [37] about the temperature and strain rate dependent deformation of HEAs. Here, it's found that the temperature dependent flow stress is also strain dependent, due to the combined environmental temperature effect and specimen self-heating effect. As shown in Fig. 7, the self-heating in CoCrFeNi alloy is confirmed by the experimentally measured temperature rise in the deformation at medium strain rate of

10/s. Consequently, the deformation at high strain rates is definitely accompanied by adiabatic temperature rise. The consistent constitutive relationship at high strain rates of 10, 000/s can be successfully measured using the SCS [52,53]. At a true strain less than 0.2, the dynamic flow stress increases with the increase of strain rate. With the continuous deformation, the flow stress at strain rate of 10, 000/s decreases, and agrees with that at a lower strain rate of 2600/s (Fig. 13).

The large strain testing using SCS shows the failure strain of CoCrFeNi alloy is about 100%. This corresponds to the shear deformation at an equivalent shear strain rate of  $1.73 \times 10^4/\text{s}$ , with an equivalent shear failure strain of 173%. With the assistance of SEM and EBSD techniques, the microstructural examinations confirm that the CoCrFeNi alloy fails by ASB. It's interesting to note that, ASB has not been found in HEAs upon dynamic tension [78,85] or compression [20,86]. The stress state would affect the ASB sensitivity [39,87]. When the HEAs are subjected to dynamic uniaxial compression or tension, there would be no favourable direction of shear deformation. ASB would hardly take place in HEAs under dynamic compression or tension. In contrast, ASB forms relatively easier under stress states with shear component [87,88], compared to the uniaxial compression or tension. In the present work, the macro and micro characterizations point out the strong resistance of CoCrFeNi alloy to dynamic shear failure. The adiabatic shear failure is governed by the competition between strain hardening and thermal softening. As suggested by Meyers et al. [25], the strong ASB resistance of HEA is attributed to the remarkable strain hardening capacity and relatively small thermal softening effect.

A comparison of the dynamic flow response and the energy absorption is made among the CoCrFeNi alloy and other alloys [58,71,76]. The yield stress of CoCrFeNi alloy is not as high as that of lightweight titanium alloys, but is comparable to that of 1020 structural steel. Likewise, it's found that the fracture surface and the relatively wide ASB width in CoCrFeNi HEA, are also similar to the observations in dynamically failed AISI 1018 steel [80] and AISI 4340 steel [81]. The wide ASB would indicate a strong resistance to shear localization, see Marchard and Duffy [43]. The CoCrFeNi HEA shows exceptional strain hardening and high energy absorption. These two unique properties would enable its use in impact resistant structures in armour design [27,89], and in aerospace engineering [79] if the weight can be properly reduced [90].

Future research will continue to study the adiabatic characteristics of HEAs at high strain rates. An even smaller SCS will be interesting to achieve the strain rate of  $10^5/\text{s}$ . Likewise, a comparison of the dynamic failure of HEAs with varying elements will be investigated, in order to guide the HEA design towards engineering applications.

#### 5. Conclusions

This paper reports the constitutive response of a CoCrFeNi HEA over a wide range of strain rates (and temperatures), using a hydraulic Instron machine and a bespoke SHPB synchronized with a high speed camera. The conclusions are as follows:

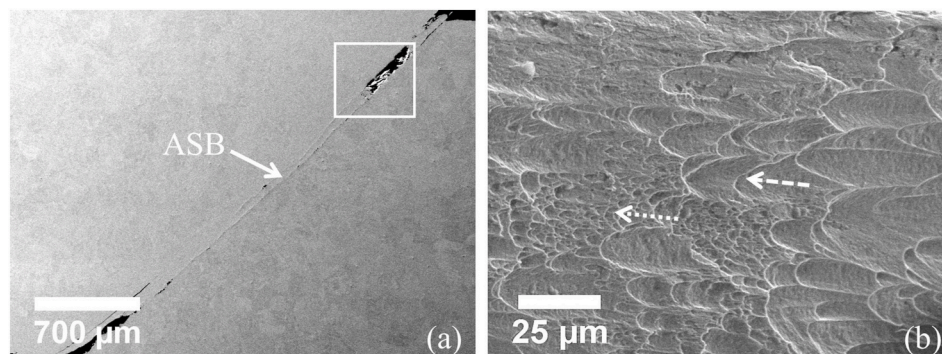


Fig. 19. Typical microstructures of CoCrFeNi at high strain rate shear loading. (a) Failure with ASB (b) Fracture surface characterization.

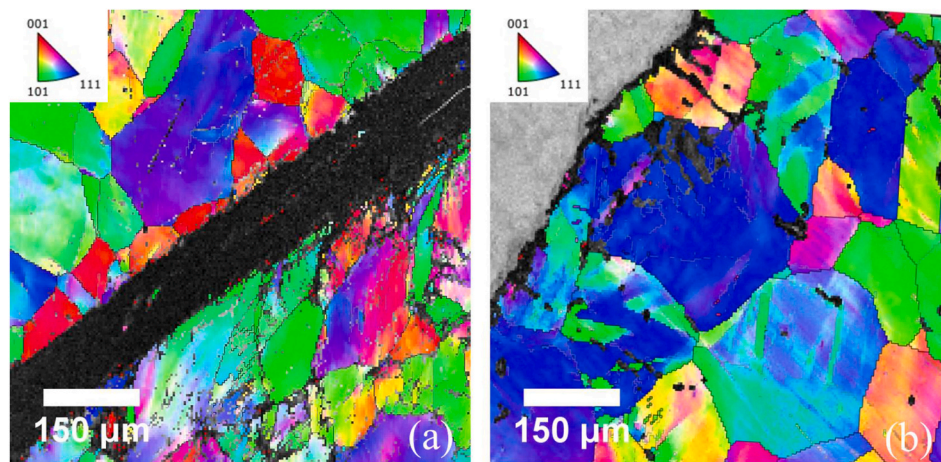


Fig. 20. EBSD maps of CoCrFeNi alloy failed in dynamic shear loading (a) ASB failure (b) Microstructure close to the shear fracture surface.

- A series of strain rates including quasi-static  $10^{-2}$ /s, medium strain rate of  $10^1$ /s, high strain rates from  $5 \times 10^2$ /s to  $1.1 \times 10^4$ /s are achieved, to measure the constitutive relationships of CoCrFeNi alloy.
- The compressive deformation of CoCrFeNi alloy at medium strain rate is with a self-heated temperature rise. This confirms the thermo-mechanical coupling characteristic of CoCrFeNi alloy at high strain rates.
- The compressive deformation process of CoCrFeNi HEA at high strain rates and various temperatures is monitored, with the assistance of high speed photography and DIC techniques. This enables accurate characterisation of the constitutive relationship of CoCrFeNi HEA at high strain rates.
- The constitutive responses of CoCrFeNi alloy show strain rate dependence. The strain hardening is affected by the strain rate. The flow stress increases with the increase of strain rate. The strain rate dependent flow stress is described by a power law model.
- The dynamic flow stress decreases from room temperature to 200 °C. The temperature effect on the dynamic flow of CoCrFeNi is also strain dependent.
- The CoCrFeNi HEA shows remarkable resistance to shear failure, with an equivalent shear strain of about 173%. The microstructural characterizations show that this CoCrFeNi HEA failed by ASB.
- It is the exceptional strain hardening and energy absorption that make the CoCrFeNi HEA unique in impact engineering applications.

#### Data availability

The raw/processed data required to reproduce these findings cannot be shared at this time due to technical or time limitations.

#### CRediT authorship contribution statement

**Longhui Zhang:** Conceptualization, Investigation, Methodology, Software, Formal analysis, Visualization, Resource, Self-supervision, Data curation, Writing – original draft, Writing – review & editing.

#### Declaration of competing interest

The author declares that they have no known competing financial interests or personal relationships that could have appeared to influence the work reported in this paper.

#### Acknowledgements

The support and fruitful suggestions from Dr. D. Townsend are

greatly appreciated. Prof. N. Petrinic is acknowledged for the 'hunting' equipment in the Laboratory. Previous discussions with Ms. L. Farquhar at The University of Sheffield and with Dr. HB. Yu at the Canadian Nuclear Laboratories are appreciated. The assistance from Mr. J. Fullerton and Dr. K. Dragnevski is acknowledged.

#### References

- [1] J.W. Yeh, S.K. Chen, S.J. Lin, J.Y. Gan, T.S. Chin, T.T. Shun, C.H. Tsau, S.Y. Chang, *Adv. Eng. Mater.* 6 (2004) 299–303.
- [2] B. Cantor, I. Chang, P. Knight, A. Vincent, *Mater. Sci. Eng. A* 375 (2004) 213–218.
- [3] A.V. Kuznetsov, D.G. Shaysultanov, N.D. Stepanov, G.A. Salishchev, O.N. Senkov, *Mater. Sci. Eng. A* 533 (2012) 107–118.
- [4] B. Gludovatz, A. Hohenwarter, D. Catoor, E.H. Chang, E.P. George, R.O. Ritchie, *Science* 345 (2014) 1153–1158.
- [5] M.A. Hemphill, T. Yuan, G. Wang, J. Yeh, C. Tsai, A. Chuang, P. Liaw, *Acta Mater.* 60 (2012) 5723–5734.
- [6] W. Zhang, P.K. Liaw, Y. Zhang, *Sci. China Mater.* 61 (2018) 2–22.
- [7] Y. Zhang, T.T. Zuo, Z. Tang, M.C. Gao, K.A. Dahmen, P.K. Liaw, Z.P. Lu, *Prog. Mater. Sci.* 61 (2014) 1–93.
- [8] C. Li, Y. Xue, M. Hua, T. Cao, L. Ma, L. Wang, *Mater. Des.* 90 (2016) 601–609.
- [9] G. Mirone, R. Barbagallo, F. Giudice, S. Di Bella, *Mater. Sci. Eng. A* 793 (2020) 139916.
- [10] P. Siegkas, V. Tagarielli, N. Petrinic, L. Lefebvre, *J. Mater. Sci.* 46 (2011) 2741–2747.
- [11] G. Whiteman, S. Case, J.C.F. Millett, M.J. Cox, P. Avraam, J.P. Dear, A. Sancho, P. A. Hooper, *Mater. Sci. Eng. A* 759 (2019) 70–77.
- [12] A. Sancho, M.J. Cox, T. Cartwright, P.A. Hooper, J.P. Dear, C.M. Davies, *Pressure Vessels and Piping Conference*, American Society of Mechanical Engineers, 2018. V06AT06A029.
- [13] M.A. Meyers, *Dynamic Behavior of Materials*, John Wiley & Sons, 1994.
- [14] J. He, Q. Wang, H. Zhang, L. Dai, T. Mukai, Y. Wu, X. Liu, H. Wang, T.-G. Nieh, Z. Lu, *Sci. Bull.* 63 (2018) 362–368.
- [15] E. Cadoni, D. Forni, R. Gieleta, L. Kruska, *Eur. Phys. J. Spec. Top.* 227 (2018) 29–43.
- [16] B. Hopkinson, *Philos. Trans. R. Soc. Lond. - Ser. A Contain. Pap. a Math. or Phys. Character* 213 (1914) 437–456.
- [17] H. Kolsky, *Proc. Phys. Soc. B* 62 (1949) 676.
- [18] J.M. Park, J. Moon, J.W. Bae, M.J. Jang, J. Park, S. Lee, H.S. Kim, *Mater. Sci. Eng. A* 719 (2018) 155–163.
- [19] S. Ma, Z. Jiao, J. Qiao, H. Yang, Y. Zhang, Z. Wang, *Mater. Sci. Eng. A* 649 (2016) 35–38.
- [20] S. Zhang, Z. Wang, H. Yang, J. Qiao, Z. Wang, Y. Wu, *Intermetallics* 121 (2020) 106699.
- [21] N. Kumar, Q. Ying, X. Nie, R. Mishra, Z. Tang, P. Liaw, R. Brennan, K. Doherty, K. Cho, *Mater. Des.* 86 (2015) 598–602.
- [22] T. Chereches, P. Lixandru, V. Geantă, I. Voiculescu, D. Dragnea, R. Ștefănoiu, *Applied Mechanics and Materials*, Trans Tech Publ, 2015, pp. 724–729.
- [23] V. Geantă, I. Voiculescu, R. Ștefănoiu, T. Chereches, T. Zecheru, L. Matache, A. Rotariu, *IOP Conference Series: Materials Science and Engineering*, IOP Publishing, 2018, 012041.
- [24] S. Muskeri, D. Choudhuri, P.A. Jannotti, B.E. Schuster, J.T. Lloyd, R.S. Mishra, S. Mukherjee, *Adv. Eng. Mater.* 22 (2020) 2000124.
- [25] M.A. Meyers, Z. Li, S. Zhao, B. Wang, Y. Liu, P.K. Liaw, *EPJ Web of Conferences*, EDP Sciences, 2018, 03028.
- [26] Z. Li, S. Zhao, S.M. Alotaibi, Y. Liu, B. Wang, M.A. Meyers, *Acta Mater.* 151 (2018) 424–431.
- [27] A. Serjouei, R. Chi, Z. Zhang, I. Sridhar, *Int. J. Impact Eng.* 77 (2015) 30–41.

- [28] S. Jia, F. Wang, L. Yu, Z. Wei, B. Xu, *Sci. Prog.* 103 (2020), 0036850419877744.
- [29] W. Cao, Y. Wang, P. Zhou, X. Yang, K. Wang, B. Pang, R. Chi, Z. Su, *Int. J. Mech. Sci.* 163 (2019) 105097.
- [30] F. Wang, Z. Yue, *Mater. Des.* 31 (2010) 687–695.
- [31] K.S. Carney, J.M. Pereira, D.M. Revilock, P. Matheny, *Int. J. Impact Eng.* 36 (2009) 720–728.
- [32] J.B. Husband, University of Saskatchewan, 2007.
- [33] D. Rittel, S. Lee, G. Ravichandran, *Exp. Mech.* 42 (2002) 58–64.
- [34] D. Rittel, G. Ravichandran, S. Lee, *Mech. Mater.* 34 (2002) 627–642.
- [35] A. Dorogoy, D. Rittel, A. Godinger, *Exp. Mech.* 5 (2015) 1627–1639.
- [36] J. Peng, L. Li, F. Li, B. Liu, S. Zharebtsov, Q. Fang, J. Li, N. Stepanov, Y. Liu, F. Liu, P.K. Liaw, *Int. J. Plast.* 145 (2021) 103073.
- [37] L. Li, H. Chen, Q. Fang, J. Li, F. Liu, Y. Liu, P.K. Liaw, *Intermetallics* 120 (2020) 106741.
- [38] Z. Xie, W.-R. Jian, S. Xu, I.J. Beyerlein, X. Zhang, Z. Wang, X. Yao, *Acta Mater.* 221 (2021) 117380.
- [39] B. Yilong, B. Dodd, *Adiabatic Shear Localization: Occurrence, Theories, and Applications*, Pergamon Press, 1992.
- [40] D. Rittel, L. Zhang, S. Osovski, *Phys. Rev. Appl.* 7 (2017), 044012.
- [41] S. Walley, *Metall. Mater. Trans.* 38 (2007) 2629–2654.
- [42] R. Winter, *Phil. Mag.* 31 (1975) 765–773.
- [43] A. Marchand, J. Duffy, *J. Mech. Phys. Solid.* 36 (1988) 251–283.
- [44] D. Rittel, Z. Wang, *Mech. Mater.* 40 (2008) 629–635.
- [45] T. Chu, W. Ranson, M.A. Sutton, *Exp. Mech.* 25 (1985) 232–244.
- [46] S. Daly, D. Rittel, K. Bhattacharya, G. Ravichandran, *Exp. Mech.* 49 (2009) 225–233.
- [47] R. Yang, H. Zhang, L. Shen, Y. Xu, Y. Bai, B. Dodd, *Phil. Trans. Math. Phys. Eng. Sci.* 372 (2014) 20130208.
- [48] S. Xia, Y. Zhang, *Mater. Sci. Eng. A* 733 (2018) 408–413.
- [49] M. Seifi, D. Li, Z. Yong, P.K. Liaw, J.J. Lewandowski, *JOM* 67 (2015) 2288–2295.
- [50] M. Vaidya, K. Pradeep, B. Murty, G. Wilde, S. Divinski, *Acta Mater.* 146 (2018) 211–224.
- [51] X. Qin, C.H. Shek, *Acta Metall. Sin.* (2021) 1–8.
- [52] D. Rittel, A. Bhattacharyya, B. Poon, J. Zhao, G. Ravichandran, *Mater. Sci. Eng. A* 447 (2007) 65–70.
- [53] M. Vural, D. Rittel, G. Ravichandran, *Metal. Mater. Transac. Phys. Metal. Mater. Sci.* 34A (2003) 2873–2885.
- [54] V. Abaqus, Dassault Systemes Simulia Corporation, 2014, p. 651.
- [55] A. Dorogoy, D. Rittel, *Exp. Mech.* 45 (2005) 167–177.
- [56] A. Dorogoy, D. Rittel, *Exp. Mech.* 45 (2005) 178–185.
- [57] D. Rittel, Z. Wang, A. Dorogoy, *Int. J. Impact Eng.* 35 (2008) 1280–1292.
- [58] L. Zhang, A. Pellegrino, D. Townsend, N. Petrinic, *Int. J. Mech. Sci.* 189 (2020) 105970.
- [59] L. Zhang, D. Townsend, N. Petrinic, A. Pellegrino, *Int. J. Impact Eng.* 158 (2021) 104026.
- [60] L. Zhang, D. Townsend, N. Petrinic, A. Pellegrino, *Compos. Struct.* 280 (2022) 114853.
- [61] L. Zhang, D. Townsend, N. Petrinic, A. Pellegrino, *Compos. B. Eng.* 234 (2022) 109738.
- [62] A. Pellegrino, F. De Cola, K. Dragnevski, N. Petrinic, *J. Dynam. Behav. Mater.* 2 (2016) 438–451.
- [63] L. GmbH, LaVision GmbH Göttingen, 2015.
- [64] G.T. Gray III, Classic split-hopkinson pressure bar testing, in: H. Kuhn, D. Medlin (Eds.), *Mechanical Testing and Evaluation*, ASM International, 2000, 0.
- [65] M. Vural, D. Rittel, *Exp. Tech.* 27 (2003) 35–39.
- [66] F. De Cola, A. Pellegrino, C. Glöfner, D. Penumadu, N. Petrinic, *Exp. Mech.* 58 (2018) 223–242.
- [67] L. Pochhammer, *J. für die Reine Angewandte Math. (Crelle's J.)* 81 (1876) 324–336.
- [68] P. Follansbee, C. Frantz, *J. Eng. Mater. Technol.* 105 (1983) 61–66.
- [69] B.A. Boley, J.H. Weiner, *Theory of Thermal Stresses*, Courier Corporation, 2012.
- [70] D. Rittel, *Mech. Mater.* 31 (1999) 131–139.
- [71] D. Rittel, L.H. Zhang, S. Osovski, *J. Mech. Phys. Solid.* 107 (2017) 96–114.
- [72] D. Macdougall, J. Harding, *Int. J. Impact Eng.* 21 (1998) 473–488.
- [73] D. Macdougall, *Exp. Mech.* 40 (2000) 298–306.
- [74] S. Wang, T. Zhang, H. Hou, Y. Zhao, *Phys. Status Solidi* 255 (2018) 1800306.
- [75] T. Zhang, S. Ma, D. Zhao, Y. Wu, Y. Zhang, Z. Wang, J. Qiao, *Int. J. Plast.* 124 (2020) 226–246.
- [76] L. Zhang, D. Rittel, S. Osovski, *Mater. Sci. Eng., A* 729 (2018) 94–101.
- [77] S. Walley, W. Proud, P. Rae, J. Field, *Rev. Sci. Instrum.* 71 (2000) 1766–1771.
- [78] K. Wang, X. Jin, Y. Zhang, P.K. Liaw, J. Qiao, *Phys. Rev. Mater.* 5 (2021) 113608.
- [79] Rolls-Royce Plc, the Jet Engine, John Wiley & Sons, 2015.
- [80] K. Hartley, J. Duffy, R. Hawley, *J. Mech. Phys. Solid.* 35 (1987) 283–301.
- [81] A. Odeshi, M. Bassim, S. Al-Ameeri, Q. Li, *J. Mater. Process. Technol.* 169 (2005) 150–155.
- [82] M. Zhou, A.J. Rosakis, G. Ravichandran, *J. Mech. Phys. Solid.* 44 (1996) 981–1006.
- [83] J. Johansson, C. Persson, H. Lai, M.H. Colliander, *Mater. Sci. Eng. A* 662 (2016) 363–372.
- [84] T. Kozmel, M. Vural, S. Tin, *J. Mater. Sci.* 51 (2016) 7554–7570.
- [85] Y. Wang, Z. Jiao, G. Bian, H. Yang, H. He, Z. Wang, P. Liaw, J. Qiao, *Mater. Sci. Eng. A* 839 (2022) 142837.
- [86] L. Wang, J.W. Qiao, S.G. Ma, Z.M. Jiao, T.W. Zhang, G. Chen, D. Zhao, Y. Zhang, Z. H. Wang, *Mater. Sci. Eng. A* 727 (2018) 208–213.
- [87] Z. Wei, J. Yu, J. Li, Y. Li, S. Hu, *Int. J. Impact Eng.* 26 (2001) 843–852.
- [88] K. Ramesh, *Mech. Mater.* 17 (1994) 165–173.
- [89] E. Cadoni, M. Dotta, D. Forni, H. Kaufmann, *Procedia Eng.* 197 (2017) 168–175.
- [90] R. Feng, M.C. Gao, C. Lee, M. Mathes, T. Zuo, S. Chen, J.A. Hawk, Y. Zhang, P. K. Liaw, *Entropy* 18 (2016) 333.